A&A 550, A96 (2013)
DOI: 10.1051/0004-6361/201220519

Astronomy & Astrophysics

The chemistry of ions in the Orion Bar I. – CH^+, SH^+, and CF^+ ⋆

The effect of high electron density and vibrationally excited H_2 in a warm PDR surface

Z. Nagy[1,2], F. F. S. Van der Tak[2,1], V. Ossenkopf[3], M. Gerin[4], F. Le Petit[5], J. Le Bourlot[5], J. H. Black[6], J. R. Goicoechea[7], C. Joblin[8,9], M. Röllig[3], and E. A. Bergin[10]

[1] Kapteyn Astronomical Institute, PO Box 800, 9700 AV, Groningen, The Netherlands
e-mail: nagy@astro.rug.nl
[2] SRON Netherlands Institute for Space Research, PO Box 800, 9700 AV, Groningen, The Netherlands
[3] I. Physikalisches Institut der Universität zu Köln, Zülpicher Straße 77, 50937 Köln, Germany
[4] LERMA, UMR 8112 du CNRS, Observatoire de Paris, École Normale Supérieure, France
[5] Observatoire de Paris, LUTH and Université Denis Diderot, Place J. Janssen, 92190 Meudon, France
[6] Chalmers University of Technology, Department of Earth and Space Sciences, Onsala Space Observatory, 43992 Onsala, Sweden
[7] Centro de Astrobiología, CSIC-INTA, 28850 Madrid, Spain
[8] Université de Toulouse, UPS-OMP, IRAP, Toulouse, France
[9] CNRS, IRAP, 9 Av. Colonel Roche, BP 44346, 31028 Toulouse Cedex 4, France
[10] Department of Astronomy, The University of Michigan, 500 Church Street, Ann Arbor, MI 48109-1042, USA

Received 8 October 2012 / Accepted 12 December 2012

ABSTRACT

Context. The abundances of interstellar CH^+ and SH^+ are not well understood as their most likely formation channels are highly endothermic. Several mechanisms have been proposed to overcome the high activation barriers, including shocks, turbulence, and H_2 vibrational excitation.
Aims. Using data from the *Herschel* Space Observatory, we studied the formation of ions, in particular CH^+ and SH^+ in a typical high UV-illumination warm and dense photon-dominated region (PDR), the Orion Bar.
Methods. The HIFI instrument on board *Herschel* provides velocity-resolved line profiles of CH^+ 1–0 and 2–1 and three hyperfine transitions of SH^+ 1_2–0_1. The PACS instrument provides information on the excitation and spatial distribution of CH^+ by extending the observed CH^+ transitions up to J = 6–5. We compared the observed line intensities to the predictions of radiative transfer and PDR codes.
Results. All CH^+, SH^+, and CF^+ lines analyzed in this paper are seen in emission. The widths of the CH^+ 2–1 and 1–0 transitions are of ∼5 km s^{-1}, significantly broader than the typical width of dense gas tracers in the Orion Bar (∼2–3 km s^{-1}) and are comparable to the width of species that trace the interclump medium such as C^+ and HF. The detected SH^+ transitions are narrower compared to CH^+ and have line widths of ∼3 km s^{-1}, indicating that SH^+ emission mainly originates in denser condensations. Non-LTE radiative transfer models show that electron collisions affect the excitation of CH^+ and SH^+ and that reactive collisions need to be taken into account to calculate the excitation of CH^+. Comparison to PDR models shows that CH^+ and SH^+ are tracers of the warm surface region (A_V < 1.5) of the PDR with temperatures between 500 and 1000 K. We have also detected the 5–4 transition of CF^+ at a width of ∼1.9 km s^{-1}, consistent with the width of dense gas tracers. The intensity of the CF^+ 5–4 transition is consistent with previous observations of lower-J transitions toward the Orion Bar.
Conclusions. An analytic approximation and a numerical comparison to PDR models indicate that the internal vibrational energy of H_2 can explain the formation of CH^+ for typical physical conditions in the Orion Bar near the ionization front. The formation of SH^+ is also likely to be explained by H_2 vibrational excitation. The abundance ratios of CH^+ and SH^+ trace the destruction paths of these ions, and indirectly, the ratios of H, H_2, and electron abundances as a function of depth into the cloud.

Key words. ISM: molecules – ISM: individual objects: Orion Bar

1. Introduction

The methylidyne cation CH^+ was one of the first molecules to be detected in the interstellar medium (Douglas & Herzberg 1941). Early studies of CH^+ found its abundance to be consistently larger than the predictions of steady-state chemical models in quiescent molecular clouds (e.g. Van Dishoeck & Black 1986). One of the possible formation routes is the endothermic reaction $C^+ + H_2 + 0.41$ eV $\rightarrow CH^+ + H$. To reproduce the observed CH^+ abundances, several mechanisms have been proposed to overcome the high activation barrier of the formation reaction. For low-density diffuse interstellar clouds, C-shocks (Pineau des Forêts et al. 1986) and turbulent dissipation (Godard et al. 2009) have been proposed and confirmed by Falgarone et al. (2010a,b) and Godard et al. (2012). Alternatively, in denser regions with strong far-ultraviolet (FUV) radiation fields, the internal energy available in the vibrationally excited H_2 molecules

⋆ *Herschel* is an ESA space observatory with science instruments provided by European-led Principal Investigator consortia and with important participation from NASA.

has been proposed to help overcome the large activation barrier (Sternberg & Dalgarno 1995; Agundez et al. 2010).

Sulfanylium (SH^+) has a similar chemistry to CH^+, having a formation route via S^+ and H_2; however, this reaction is twice as endothermic as the CH^+ formation reaction. After non-detections of SH^+ in the UV domain in the spectra of nearby stars (Millar & Hobbs 1988; Magnani & Salzer 1989, 1991), the 526 GHz $N_J = 1_2–0_1$ transition of SH^+ has been detected in emission using *Herschel* toward the high-mass protostar W3 IRS 5 (Benz et al. 2010). The 526 GHz transition has also been detected in absorption in the diffuse interstellar medium towards various distant star-forming regions (Godard et al. 2012). The 683 GHz transition of SH^+ has been detected in absorption towards Sgr B2(M) from the ground with the Carbon Heterodyne Array of the MPIfR (CHAMP+) receiver of the Atacama Pathfinder Experiment 12 m telescope (APEX; Menten et al. 2011).

In this paper, we study the formation and excitation of CH^+ and SH^+ in a prototypical photon-dominated region (PDR), the Orion Bar. The Orion Bar is located at a distance of 414 pc (Menten et al. 2007). Its stratified structure has been the subject of many previous studies (such as Van der Wiel et al. 2009 and references therein). The mean density of the Orion Bar is about $\gtrsim 10^5$ cm^{-3}, the mean molecular gas temperature 85 K (Hogerheijde et al. 1995), and the impinging radiation field is $(1–4) \times 10^4$ in Draine units (Draine field: $\chi = 2.7 \times 10^{-3}$ erg s^{-1} cm^{-2} for the energy range $6 < h\nu < 13.6$ eV; Draine 1978). Most of the low-J molecular line emission originates in an interclump medium with a density between a few 10^4 and 2×10^5 cm^{-3} (Simon et al. 1997). High-density tracers such as HCN and $H^{13}CN$ originate in dense clumps, as confirmed by interferometric observations (Young Owl et al. 2000). The density of the clumps is in the range between 1.5×10^6 and 6×10^6 cm^{-3} (Lis & Schilke 2003). Apart from the large clumps detected in $H^{13}CN$ deep inside the Bar, small, warm ($T_{kin} \sim 160–220$ K), and dense ($n_H \sim 10^{6–7}$ cm^{-3}) condensations have been suggested to explain the excited OH emission at the PDR surface (Goicoechea et al. 2011).

This paper aims to characterize the medium where ions such as CH^+ and SH^+ form and to distinguish between the mechanisms that can overcome the high activation barriers of the formation reaction in a warm and dense PDR. We also report the detection of the CF^+ 5–4 transition. We will address another ion, OH^+ in a separate paper (Van der Tak et al., in prep.).

2. Observations and data reduction

The CO^+ peak ($\alpha_{J2000} = 05^h35^m20.6^s$, $\delta_{J2000} = -05°25'14''$) in the Orion Bar (Störzer et al. 1995) has been observed as part of the *Herschel* observations of EXtra-Ordinary Sources (HEXOS) guaranteed-time key program (Bergin et al. 2010) for the Heterodyne Instrument for the Far-Infrared (HIFI, De Graauw et al. 2010) of the *Herschel* Space Observatory (Pilbratt et al. 2010) in every HIFI band as a spectral scan. The data were reduced using the *Herschel* interactive processing environment (HIPE, Ott et al. 2010) pipeline version 6.0. The velocity calibration of HIFI data is accurate to ~0.5 km s^{-1} or better. The sideband deconvolution was done using the *doDeconvolution* task in HIPE. In this paper we use the HIFI bands 1a, 1b, 2a and 3a from the HEXOS spectral line survey. These observations were carried out in March and April 2011 in load chop mode with a redundancy of 4 and had total integration times of 2.4 h, 2.2 h, 3.1 h, and 1.3 h, respectively. The Wide-Band Spectrometer (WBS) backend was used which covers 4 GHz bandwidth in four 1140 MHz subbands at 1.1 MHz resolution.

In addition to HIFI spectral scans observed as a part of the HEXOS key program, the CH^+ 2–1 transition was observed as a deep integration in a spectral scan in band 6b, with a total integration time of 11.7 h and a redundancy 4 in dual-beam-switch (DBS) mode. Both WBS and the High Resolution Spectrometer (HRS) backends were used. It was reduced using HIPE pipeline version 8.0.

Besides the HIFI data, we used observations of the CH^+ 3–2, 4–3, 5–4, and 6–5 transitions from the Photodetector Array Camera and Spectrometer (PACS, Poglitsch et al. 2010) on board *Herschel*. The PACS observations were carried out in September 2010 and consist of two spectral scans in Range Spectroscopy mode with 5 range repetitions each (Joblin et al., in prep.). The PACS spectrometer provides 25 spectra over a $47'' \times 47''$ field-of-view resolved in 5×5 spatial pixels ("spaxels"), each with a size of ~9.4″ in the sky. The measured width of the spectrometer point spread function (PSF) is relatively constant at $\lambda \lesssim 100$ μm, but it significantly increases above the spaxel size for longer wavelengths. The resolving power varies between $\lambda/\Delta\lambda \sim 1000$ (R1 grating order) and ~5000 (B3A grating order). The central spaxel was centered at the same HIFI survey position. Observations were carried out in the "chop-nodded" mode with the largest chopper throw of 6 arcmin. The total integration time was 3.2 h for the 1342204117 observation (B2B and R1) and 2.7 h for the 1342204118 observation (B3A). PACS data were processed using HIPE 6.0.3.

Table 1 shows the spectroscopic and observational parameters of the transitions used in this paper. The rest frequencies are based on the Cologne Database for Molecular Spectroscopy (CDMS database, Müller et al. 2005). In particular, the frequencies of the CH^+ 1–0 and 2–1 and $^{13}CH^+$ 1–0 transitions are based on Müller (2010).

Table 2 includes the observed line parameters for our line sample observed with HIFI, which have been corrected for main beam efficiencies based on Roelfsema et al. (2012). In the case of the detected HIFI transitions we use the average of H- and V-polarizations. The detected lines show similar line profiles in both polarizations. The intensity difference between the polarizations is 12% for CH^+ $J = 1–0$, 8% for CH^+ $J = 2–1$, ~20% for SH^+ $N_J = 1_2–0_1$, and ~30% for CF^+ 5–4. To compare the line intensities of the transitions detected with HIFI with different beam sizes, we convert all the observed line intensities to a common ~47″ resolution. We derive conversion factors between the original beam sizes and ~47″ based on the integrated intensity map of the HCN 4–3 transition from the *James Clerk Maxwell* Telescope (JCMT) Spectral Legacy Survey (Van der Wiel et al. 2009). For this, we assume the intensity distribution of the HCN 4–3 transition to trace the spatial structure of the Orion Bar. For the PACS data (Table 2), because of uncertainties in the PSF-correction, we use the mean value of the intensity measured at the central spaxel ($I_{central}$) and that corresponding to the value integrated over 3×3 spaxels around the center ($I_{3\times3}$). The corresponding error bars are the difference between $I_{central}$ and $I_{3\times3}$. This method provides the correct agreement between Spectral and Photometric Imaging Receiver (SPIRE, Griffin et al. 2010) and HIFI data for CO lines (Joblin et al., in prep.). The large (40%) error bar corresponding to the intensity of the 5–4 transition is caused by the presence of oscillations (fringes) in this range. Owing to a lower band intensity and a significant noise level, only $I_{3\times3}$ was measured for the intensity of the 6–5 transition; $I_{central}$ was then estimated using a standard error value.

Table 1. Spectroscopic and observational parameters of the transitions used in this paper.

Transition	Frequency (MHz)	E_{up} (K)	A (s^{-1})	Instrument/band	Beam-size ($''$)	η_{mb}
CH^+ 1–0	835 137.5	40.1	6.36×10^{-3}	HIFI, band 3a	26.5	0.75
CH^+ 2–1	1 669 281.3	120.2	6.10×10^{-2}	HIFI, band 6b	15.0	0.72
CH^+ 3–2	2 501 440.5	240.2	2.20×10^{-1}	PACS	9.4[1]	
CH^+ 4–3	3 330 629.7	400.1	5.38×10^{-1}	PACS	9.4[1]	
CH^+ 5–4	4 155 872.0	599.5	1.07	PACS	9.4[1]	
CH^+ 6–5	4 976 201.4	838.3	1.86	PACS	9.4[1]	
$^{13}CH^+$ 1–0	830216.1	39.9	5.83×10^{-3}	HIFI, band 3a	26.5	0.75
SH^+ $N_J = 1_2$–0_1, $F = 3/2$–$1/2$	526 038.7	25.3	7.99×10^{-4}	HIFI, band 1a	44.2	0.76
SH^+ $N_J = 1_2$–0_1, $F = 5/2$–$3/2$	526 047.9	25.3	9.59×10^{-4}	HIFI, band 1a	44.2	0.76
SH^+ $N_J = 1_2$–0_1, $F = 3/2$–$3/2$	526 124.9	25.3	1.60×10^{-4}	HIFI, band 1a	44.2	0.76
SH^+ $N_J = 1_1$–0_1, $F = 3/2$–$1/2$	683 336.1	32.8	2.90×10^{-4}	HIFI, band 2a	33.2	0.75
SH^+ $N_J = 1_1$–0_1, $F = 1/2$–$1/2$	683 362.0	32.8	1.16×10^{-3}	HIFI, band 2a	33.2	0.75
SH^+ $N_J = 1_1$–0_1, $F = 3/2$–$3/2$	683 422.3	32.8	1.45×10^{-3}	HIFI, band 2a	33.2	0.75
SH^+ $N_J = 1_1$–0_1, $F = 1/2$–$3/2$	683 448.2	32.8	5.79×10^{-4}	HIFI, band 2a	33.2	0.75
CF^+ 5–4	512 846.5	73.8	8.21×10^{-4}	HIFI, band 1a	44.2	0.76
CF^+ 6–5	615 365.6	103.4	1.44×10^{-3}	HIFI, band 1b	44.2	0.76
$^{13}CF^+$ 5–4	488 664.3	70.0	7.10×10^{-4}	HIFI, band 1a	44.2	0.76

Notes. [(1)] The size of one PACS spaxel.

Table 2. Detected CH^+, SH^+, and CF^+ transitions; Gaussian fit parameters for the velocity-resolved transitions observed with HIFI and PACS; and upper limits for non-detections of other CF^+ and SH^+ transitions.

Line	$\int T_{MB}\,dV$ (K km s^{-1})	V_{LSR} (km s^{-1})	ΔV (km s^{-1})	T_{peak} (K)	rms (T_{MB}) (K)
CH^+ 1–0	24.9 ± 0.20	10.5 ± 0.02	5.46 ± 0.04	4.28 ± 0.15	0.12
CH^+ 2–1	10.6 ± 0.20	10.4 ± 0.05	4.57 ± 0.11	2.18 ± 0.22	0.23
CH^+ 3–2	2.19 ± 0.31				
CH^+ 4–3	1.01 ± 0.19				
CH^+ 5–4	0.42 ± 0.15				
CH^+ 6–5	0.17 ± 0.06				
$^{13}CH^+$ 1–0[1]	0.46 ± 0.11	11.39 ± 0.15	1.30 ± 0.34	0.34 ± 0.10	0.15
SH^+ $N_J = 1_2$–0_1 $F = 3/2$–$1/2$	0.34 ± 0.02	10.92 ± 0.09	3.00[2]	0.11 ± 0.02	0.02
SH^+ $N_J = 1_2$–0_1 $F = 5/2$–$3/2$	0.57 ± 0.02	10.84 ± 0.06	3.00[2]	0.18 ± 0.02	0.02
SH^+ $N_J = 1_2$–0_1 $F = 3/2$–$3/2$	0.14 ± 0.02	10.34 ± 0.24	3.00[2]	0.04 ± 0.01	0.02
SH^+ $N_J = 1_1$–0_1 $F = 3/2$–$1/2$	≤0.18			≤0.15[3]	
SH^+ $N_J = 1_1$–0_1 $F = 1/2$–$1/2$	≤0.11			≤0.09[3]	
SH^+ $N_J = 1_1$–0_1 $F = 3/2$–$3/2$	≤0.13			≤0.12[3]	
SH^+ $N_J = 1_1$–0_1 $F = 1/2$–$3/2$	≤0.11			≤0.09[3]	
CF^+ 5–4	0.20 ± 0.02	11.13 ± 0.11	1.96 ± 0.21	0.10 ± 0.01	0.02
CF^+ 6–5	≤0.08			≤0.08[3]	
$^{13}CF^+$ 5–4	≤0.05			≤0.05[3]	

Notes. The CH^+ $J = 3$–2, 4–3, 5–4, and 6–5 transitions are spectrally unresolved from PACS. The parameters from HIFI are based on the average spectrum of H- and V-polarizations, unless otherwise specified. [(1)] Based on V-polarization data only. [(2)] Fixed parameter in the fit. [(3)] $3\times$rms noise level.

3. Results

3.1. The detected CH^+, SH^+, and CF^+ transitions

Figure 2 shows the velocity-resolved CH^+ transitions that were detected with significantly broad lines (~5 km s^{-1}) compared to the line width of dense gas tracers in the Orion Bar (~2–3 km s^{-1}, Hogerheijde et al. 1995 and an example of the CO 16–15 transition in Fig. 2). The line width of the CH^+ 2–1 and 1–0 transitions is not only significantly larger than the width of dense gas tracers, but also of species that trace a similar region to CH^+, such as CO^+ (Störzer et al. 1995; Fuente et al. 2003). The 5 km s^{-1} is comparable to the width of tracers of the interclump medium, such as C^+ ($\Delta v \sim 3.8$ km s^{-1}, also shown in Fig. 2) and HF ($\Delta v \sim 4.9$ km s^{-1}, Van der Tak et al. 2012).

Other non velocity-resolved transitions from PACS, such as the $J = 3$–2 transition (Fig. 1), show extended emission detected over all PACS spaxels, decreasing with distance from the ionization front. The maximum CH^+ 3–2 emission is seen farther into the nearly edge-on PDR compared to the peak H_2 $v = 1$–0 emission (Fig. 1). As CH^+ forms via a reaction between C^+ and H_2^*, we compare the CH^+ 3–2 intensity distribution to C^+ emission from Fig. 4 in Ossenkopf et al. (2013). The C^+ peak matches the

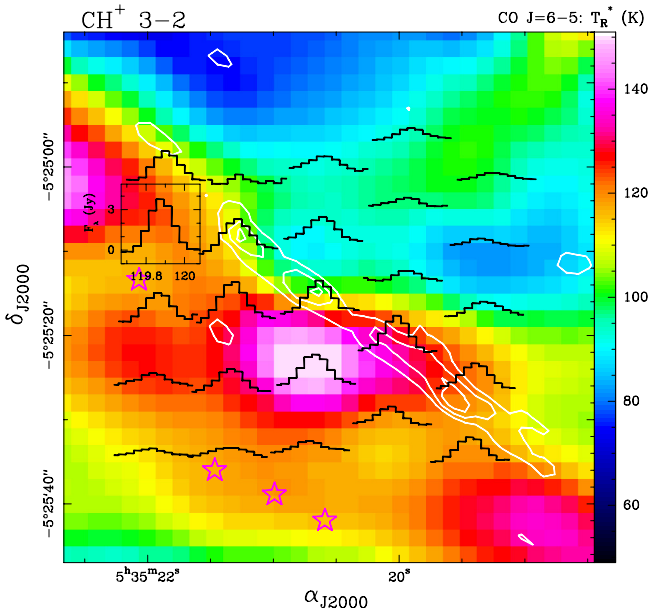

Fig. 1. PACS CH^+ 3–2 lines (black, centered on the CO^+ peak) overlaid on the distribution of the CO J = 6–5 peak brightness temperature (color image) observed with the CSO telescope at ∼11″ resolution (Lis et al. 1998). The PACS line intensity distributions are shown in units of Jy/spaxel as a function of wavelength in μm and are not velocity resolved. White contours show the brightest regions of H_2^* v = 1–0 S (1) emission (Walmsley et al. 2000). Lower-intensity H_2^* extended emission is present in the entire field (Van der Werf et al. 1996). Violet stars show the position of the $H^{13}CN$ J = 1–0 clumps deeper inside the Bar (Lis & Schilke 2003).

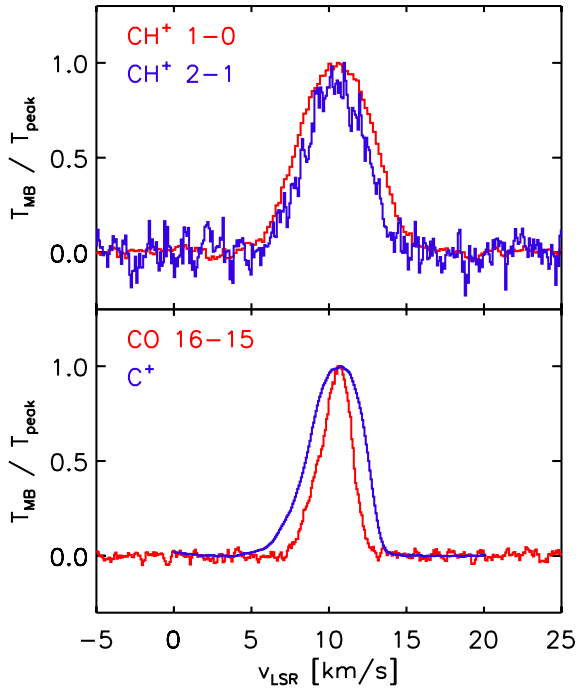

Fig. 2. *Top panel:* line profiles of CH^+ 2–1 and 1–0 transitions corresponding to the average of H- and V-polarizations observed with *Herschel*/HIFI toward the CO^+ peak in the Orion Bar. *Bottom panel:* line profiles of C^+ and CO 16–15, for comparison, observed with *Herschel*/HIFI toward the CO^+ peak in the Orion Bar.

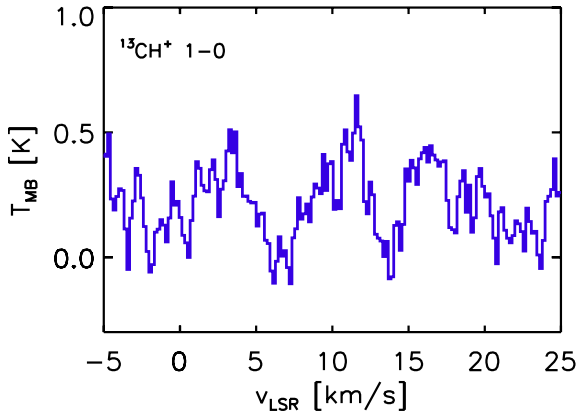

Fig. 3. Line profile of $^{13}CH^+$ 1–0 transition observed with *Herschel*/HIFI in V-polarization toward the CO^+ peak in the Orion Bar.

CH^+ peak within the HIFI beam. This indicates that CH^+ formation is limited by the C^+ abundance rather than by the H_2 excitation that is traced by the H_2 v = 1–0 S(1) emission observed by Walmsley et al. (2000).

Figure 3 shows a tentative detection of the $^{13}CH^+$ J = 1–0 in V-polarization. If it were a real detection, the observed $^{12}CH^+/^{13}CH^+$ line ratio of ∼40 would indicate an optical depth of the $^{12}CH^+$ line of ∼unity, assuming that the $^{13}CH^+$ emission is optically thin. However, this seems unlikely since a $^{12}CH^+$ optical depth of ∼1 at a temperature >100 K (see Sect. 3.2) is inconsistent with the observed $^{12}CH^+$ line intensity. Deeper observations are needed to confirm the detection of $^{13}CH^+$.

Figure 4 shows three hyperfine components of the N_J = 1_2–0_1 transition of SH^+ (F = 3/2–1/2, F = 5/2–3/2, and F = 3/2–3/2). The SH^+ F = 3/2–3/2 transition is only detected in V-polarization. The line width of the detected SH^+ transitions (3.0 km s^{-1}) is narrower than those of CH^+ and are consistent with the width of dense gas tracers in the Orion Bar, suggesting that it does not originate in the same gas component as CH^+.

We have also detected the CF^+ 5–4 transition for the first time, with a line width of ∼2 km s^{-1} (Fig. 5). The 3–2, 2–1, and 1–0 transitions of CF^+ were previously detected toward the Orion Bar from the ground by Neufeld et al. (2006) with beam sizes of HPBW = 24″, 12″, and 21″, respectively. The velocity and the width of the 5–4 transition is consistent with the parameters reported for the other detected transitions by Neufeld et al. (2006). One of the positions covered by Neufeld et al. (2006), $05^h35^m22.8^s$, −5°25′01″, is close (ΔRA ∼ 30″, ΔDec ∼ 13″) to our observed position which is within the beam of HIFI at the frequency of the 5–4 transition (∼44.2″). Assuming uniform beam-filling, a single excitation temperature of all four levels and optically thin lines, the measured line intensity is consistent with those detected by Neufeld et al. (2006) (Fig. 6) and implies a column density of $\sim 2.1 \times 10^{12}$ cm^{-2} and a rotation temperature of ∼32 K.

We derived upper limits for other non-detected CF^+ and SH^+ transitions. We estimated rms noise levels in the averaged spectrum of H- and V-polarizations; 3σ upper limits on the integrated line intensities are estimated using (e.g. Coutens et al. 2012)

$$I(3\sigma)\ [\mathrm{K\ km\ s^{-1}}] = 3\ \mathrm{rms}\ \sqrt{2\ \mathrm{d}v\ FWHM},$$

where dv is the channel width in km s^{-1} and the rms noise level is derived in a velocity range of ±5 km s^{-1} around the expected velocity. We use a full width at half maximum (FWHM) of 1.9 km s^{-1} for the $^{13}CF^+$ 5–4 (488 664.3 MHz) and the CF^+ 6–5 (615 365.6 MHz) upper limits, and $FWHM$ = 3 km s^{-1} for SH^+ N_J = 1_1–0_1 (∼683 GHz). The derived 3σ upper limits are listed in Table 2.

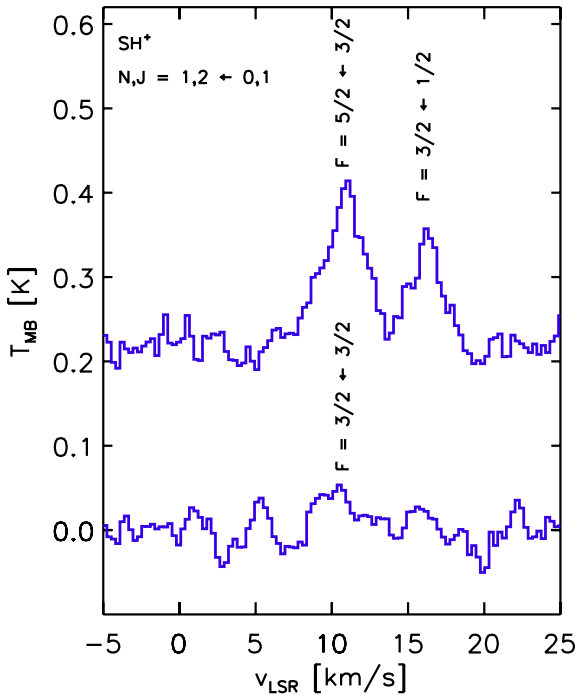

Fig. 4. Line profiles of the three hyperfine transitions of SH^+ $N_J = 1_2 - 0_1$ observed with *Herschel*/HIFI corresponding to the average of H- and V-polarizations toward the CO^+ peak in the Orion Bar.

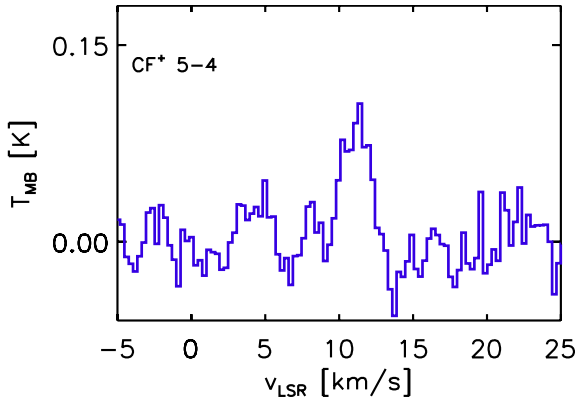

Fig. 5. Line profile of CF^+ 5–4 transition corresponding to the average of H- and V-polarizations observed with *Herschel*/HIFI toward the CO^+ peak in the Orion Bar.

3.2. Physical conditions traced by CH^+ and SH^+

To estimate molecular column densities, we use the non-LTE radiative transfer code RADEX (Van der Tak et al. 2007). We use H_2 as a collision partner for the excitation of CH^+, as we expect a significant fraction of hydrogen to be in a molecular form at the observed position. Rates for inelastic collisions between CH^+ and H are not available, but are expected to be of the same order of magnitude as the rates for inelastic collisions between CH^+ and H_2. If most H is in an atomic state, the density used as an input parameter is then the sum of n(H) and $n(H_2)$. We also include excitation via inelastic collisions between CH^+ and electrons, as the importance of excitation by electrons for HF has been recently demonstrated by Van der Tak et al. (2012). We apply an electron density of $\sim$10 cm^{-3}. This is justified, if we assume that the electron abundance is determined by the abundance of C^+. The column density of C^+ is approximately 10^{18} cm^{-2} (Ossenkopf et al. 2013) and the H_2 column density is approximately 10^{22} cm^{-2} (e.g. Habart et al. 2010; Van der Wiel et al. 2009). This implies an electron abundance of 10^{-4} and using $n(H_2) = 10^5$ cm^{-3}, an electron density of 10 cm^{-3}. In the following we consider both H_2 and electron collisions to probe the excitation of CH^+ and SH^+.

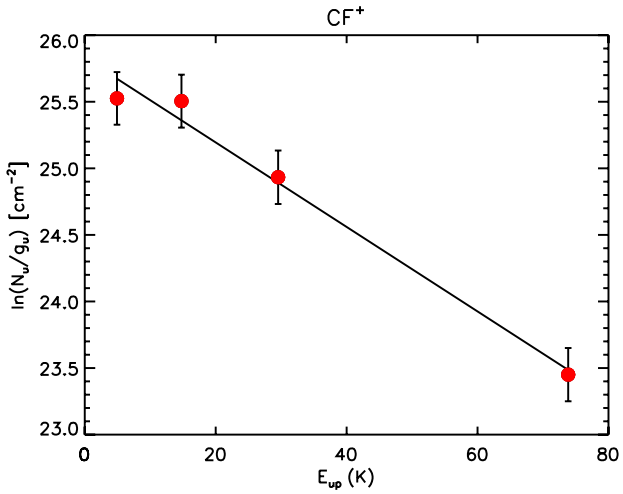

Fig. 6. Rotation diagram of CF^+ including the transitions detected by Neufeld et al. (2006).

For CH^+ our calculations are based on collision rates from Turpin et al. (2010), for temperatures in the range between 10 K and 200 K, covering transitions up to the 5–4 transition (E_{up} = 599.5 K). These rates have been scaled from CH^+ –He to CH^+–H_2 based on Schöier et al. (2005). For electron collisions, we use collision rates from Lim et al. (1999) that are available for temperatures between 100 and 15 000 K.

Collisions with H_2 and electrons are not always inelastic, but may lead to a chemical reaction. In the case of CH^+ this is important since the collision rates with H_2 and electrons are comparable to the chemical reaction rates for CH^+ with H_2 and electrons. For example, for CH^+-e^- the chemical reaction rate is 9×10^{-8} cm^3 s^{-1} for the destruction (Woodall et al. 2007) and is 6.4×10^{-7} cm^3 s^{-1} for the excitation of the $J = 1-0$ transition at 1000 K. For CH^+-H_2 the destruction rate is 1.2×10^{-9} cm^3 s^{-1} (Woodall et al. 2007) and an excitation rate is 1.1×10^{-10} cm^3 s^{-1} for the $J = 1-0$ transition at 100 K. Therefore, we consider the chemical formation and destruction rates in the statistical equilibrium calculation (e.g. Van der Tak et al. 2007). The statistical equilibrium for states $i = 1 - N$ of energy E_i that is solved using the RADEX code is given by the time-independent rate equations

$$\frac{\mathrm{d}n_i}{\mathrm{d}t} = \sum_{j \neq i}^{N} n_j P_{ji} - n_i \sum_{j \neq i}^{N} P_{ij} = \mathcal{F}_i - n_i \mathcal{D}_i \ \mathrm{cm^{-3}\ s^{-1}},$$

where

$$\begin{aligned} P_{ij} &= A_{ij} + B_{ij}\bar{J} + C_{ij} \quad (E_i > E_j) \\ &= B_{ij}\bar{J} + C_{ij} \quad (E_i < E_j) \end{aligned}$$

and A_{ij} and B_{ij} are the Einstein coefficients, $\bar{J}$ is the mean intensity at the frequency of transition $i \rightarrow j$, C_{ij} is the sum over all collision partners of the rates of inelastic, collision-induced transitions $i \rightarrow j$, n_i is the number density (cm^{-3}) of molecules in level i, and $\mathcal{D}_i$ is the rate of destruction of the molecule in level i. When detailed knowledge of the state-specific formation process is lacking, the formation rate into level i is expressed as

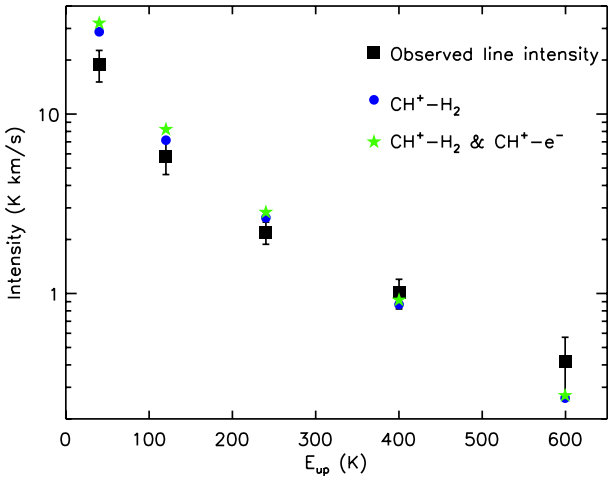

Fig. 7. Output of the RADEX models corresponding to a model with $N(CH^+) = 9 \times 10^{14}$ cm^{-2}, $n(H_2) = 10^5$ cm^{-3}, $n(e^-) = 10$ cm^{-3}, $T_{kin} = 500$ K. The blue symbols correspond to a model with excitation via collisions with H_2, the green symbols to a model with excitation via H_2 and electron collisions.

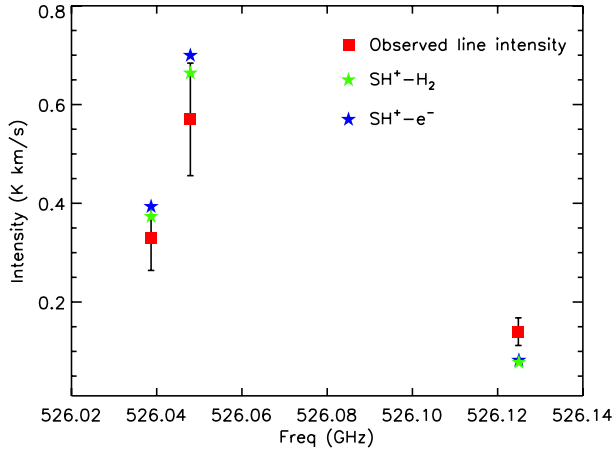

Fig. 8. Output of the RADEX models for H_2 and electron collisions compared to the observed line intensities of SH^+ for a model with $N(SH^+) = 10^{13}$ cm^{-2}, $n(H_2) = 10^6$ cm^{-3}, $n(e^-) = 10$ cm^{-3}, and $T_{kin} = 200$ K.

a Boltzmann distribution over all states at an effective formation temperature T_f

$$\mathcal{F}_i \propto g_i \exp(-E_i/kT_f),$$

where g_i is the statistical weight of level i. When the destruction rate can be estimated, as for CH^+ here, then the total formation rate is normalized so that the total number density of molecules is consistent with its column density and the density of hydrogen in steady state.

We assume that there is a balance between the formation and destruction of CH^+. To simulate the chemical pumping effect described above, i.e. the effect of destruction and subsequent formation of CH^+ in excited levels, we add an artificial level to the CH^+ level system, representing the dissociated state, that is populated with a rate equivalent to the reaction rate of CH^+-H_2 and CH^+-e^- (Woodall et al. 2007). On the formation of CH^+ through the reaction of C^+ with vibrationally excited H_2, the repopulation from the dissociated level follows a Boltzmann distribution with a formation temperature of $T_f = 9920$ K $- 4560$ K $= 5360$ K, where 4560 K is the required energy input for the endothermic CH^+ production and 9920 K is the average energy of the vibrationally excited H_2 levels following the 2-level approximation introduced by Röllig et al. (2006) where the full 15-level system was replaced by the energetically equivalent 2-level system that provides the same total vibrational heating.

Figure 7 shows the intensity predictions of two RADEX models with parameters in the range that can be expected for the Orion Bar. The error bars correspond to a 10% calibration error and a 10% error from obtaining integrated intensities by Gaussian fitting for the transitions observed with HIFI. The error bars corresponding to the PACS data are dominated by uncertainty in the PSF correction and are estimated as explained in Sect. 2. Both electron collisions and H_2 collisions suggest a kinetic temperature well above the average value (85 K) inferred for the interclump medium in the Orion Bar. Taking the formation pumping and collisional excitation described above into account, we find reasonable fits to the observed line-intensity distribution up to the 5–4 transition (the energy range for which the collision rates are available) with $N(CH^+) = 9 \times 10^{14}$ cm^{-2}, $T_{kin} = 500$ K, and $n(H_2) = 10^5$ cm^{-3}. The intensity of the 5–4 transition can be better reproduced with a kinetic temperature of $T_{kin} = 1000$ K. Temperatures between 500 K and 1000 K are expected near the edge of the cloud where the observations used in this paper have been taken. Assuming an electron density of $n_e = 10$ cm^{-3}, electron collisions mostly affect the two lowest-J transitions for $T_{kin} = 500$ K with an 10–13% increase in the intensities.

In the case of SH^+, calculations for collisions with H_2 do not exist, so we use scaled radiative rates (Black, priv. comm.) for a temperature range of 10–5000 K. We also use collision rates for electron-impact collisions calculated in the Coulomb-Born approximation (J. Black, priv. comm.), for a temperature range of 10–1000 K. Figure 8 shows the best fit models over-plotted on the observed line intensities. The error bars correspond to 20% of the observed line intensities, including calibration error and the error introduced by the estimation of the integrated intensities using a Gaussian fit. We consider lower kinetic temperatures and higher volume densities than in the case of CH^+, given that the line width suggests an origin from denser material. At the position of the CO^+ peak, warm ($T_{kin} \sim 160$–220 K) and dense (10^{6-7} cm^{-3}) condensations have been suggested to explain the OH emission. Using SH^+-H_2 collisions, a model with 10^6 cm^{-3}, $T_{kin} = 200$ K, and $N(SH^+) = 10^{13}$ cm^{-2} gives a reasonable fit to the observed line intensities (Fig. 8). In Fig. 8 we show a model with the same parameters, which includes electron collisions, assuming an electron density of $n_e = 10$ cm^{-3}. In both of these models the excitation temperatures are low (8.3–10.4 K) and the lines are optically thin ($\tau \sim 0.02$–0.2).

4. The formation of CH^+ and SH^+ via H_2 vibrational excitation

In this section we investigate the role of H_2 vibrational excitation for the formation of CH^+ and SH^+. We discuss alternative explanations in Sect. 6.

4.1. Estimate based on an analytic approximation

Testing if H_2 vibrational excitation can drive CH^+ and SH^+ formation in an environment with a given radiation field and physical parameters requires a detailed modeling with a PDR

code, with information on the chemical network and physical processes that affect the level populations of vibrationally excited H_2. A first indication can also be given using a simple analytic method to describe H_2 vibrational heating with a two level approximation (Röllig et al. 2006). The H_2 vibrational heating rate can be computed among all 15 vibrational levels in the ground electronic state, but neglecting the rotational structure, based on Eq. (C.2) in Röllig et al. (2006). A two-level system can be defined that results in the same vibrational heating rate as the full, 15-level system (Eq. (C.3), Röllig et al. 2006). The vibrationally excited "virtual" level has an upper level energy of $\Delta E_{\rm eff}$ = 9920 K. The total rate for populating this vibrationally excited level is $k_{0,1} = P_1\,\chi$, where χ is the radiation field in Draine units (Draine 1978) and $P_1 = 6.9 \times 10^{-10}$ s^{-1} is the formation rate of vibrationally excited H_2 for the defined level for a radiation field of $\chi = 1$. The de-excitation of this vibrationally excited level is via spontaneous emission, dissociation by the UV radiation field and by collisional de-excitation. The coefficient for spontaneous decay is $A_{\rm eff} = 1.9 \times 10^{-6}$ s^{-1}. The collisional de-excitation scales as $n_{\rm gas}\gamma_{\rm eff}$ with a rate coefficient of $\gamma_{\rm eff} = 5.4 \times 10^{-13}\sqrt{T}$ s^{-1} cm^{-3}. The dissociation rate is $\chi \times D_{\rm eff}$, where $D_{\rm eff} = 4.7 \times 10^{-10}$ s^{-1}. These effective coefficients $A_{\rm eff}$, $\gamma_{\rm eff}$, and $D_{\rm eff}$ for the defined 2-level system as well as the energy of the defined vibrationally excited level $\Delta E_{\rm eff}$ are obtained by considering different asymptotic values of the density n and the radiation field χ. By neglecting dissociation, the population of the vibrationally excited level is dependent on the formation rate of vibrationally excited H_2 as well as on the spontaneous decay and collisional de-excitation rates. Calculating with $n_{\rm gas} = 10^5$ cm^{-3} and $T = 500$ K for the collisional de-excitation rate, there is a balance between these processes for a radiation field of $\chi \sim 5 \times 10^3$, which gives an expected lower limit on the radiation field, above which H_2 vibrational excitation is expected to be efficient enough to drive the formation of CH^+ and SH^+. Even though neglecting dissociation introduces an additional ~10% error, this calculation shows that for the radiation field in the Orion Bar ($1–4 \times 10^4$ in Draine units), there is a large percentage of vibrationally excited H_2 to react with C^+ and form CH^+. This has been observed by Van der Werf et al. (1996) and Walmsley et al. (2000) and has already been noted for the formation of OH through the O + H_2 → OH + H reaction by Goicoechea et al. (2011). In the following section we test this idea with a more accurate approach, using PDR models.

4.2. CH^+ formation

We use the 1.4.4 version of the Meudon PDR code (Le Petit et al. 2006; Goicoechea & Le Bourlot 2007; Le Bourlot et al. 2012) to model the observed CH^+ line intensities. This version includes the Langmuir Hinshelwood and Eley-Rideal mechanisms to describe the formation of H_2 on grain surfaces. The chemical pumping effect of destruction and formation on CH^+ level populations is taken into account in addition to collisional excitation and de-excitation in the Meudon code (e.g. Gonzalez Garcia et al. 2008). The Meudon code treats CH^+ formation as described in Agundez et al. (2010)

$$H_2(j = 0 - 7) + C^+ \xrightarrow{k_1} CH^+ + H \quad (1)$$

$$H_2(v = 1) + C^+ \xrightarrow{k_2} CH^+ + H. \quad (2)$$

In reaction 1, H_2 rotational levels up to $J = 7$ are used, which has an energy, $E_7 = 4586.4$ K which is close to the activation barrier of the $H_2 + C^+ \rightarrow CH^+ + H$ reaction. We take into account the $v = 1$ vibrational level only because its energy (~5987 K) is enough to overcome the activation barrier of the CH^+ formation reaction. The formation rates are $k_1 = 1.58 \times 10^{-10} \exp(-[4827 - E_j/k]/T)$ based on Gerlich et al. (1987) and $k_2 = 1.6 \times 10^{-9}$ (Hierl et al. 1997).

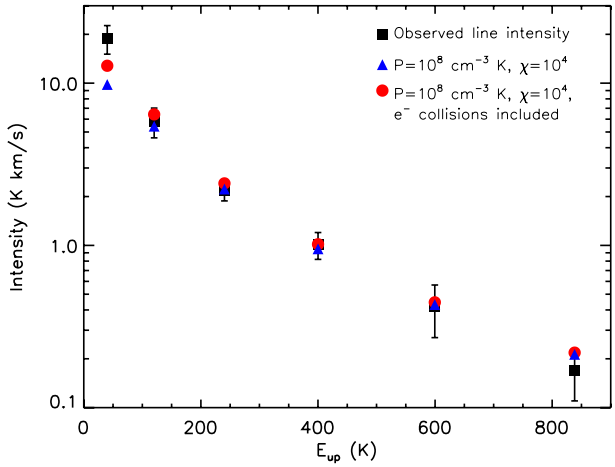

Fig. 9. CH^+ line intensities as a function of E_u, comparison between the observed line intensities and the predictions of an isobaric PDR model with a pressure of 10^8 cm^{-3} K for a radiation field of $\chi = 10^4$.

We use isobaric models for typical conditions for the Orion Bar with pressures in the range between 5×10^7 cm^{-3} K and 2×10^8 cm^{-3} K, corresponding to $T_{\rm kin} \sim 500$ K (RADEX models) and $n \sim 10^5$ cm^{-3}; and $T_{\rm kin} \sim 1000$ K (RADEX models) and $n \sim 2 \times 10^5$ cm^{-3} (typical interclump medium density, e.g. Simon et al. 1997); respectively. We apply a radiation field on the side where the cloud is illuminated from in the range between $\chi_{\rm front} = 10^4$ and 3×10^4 in Draine units (Draine 1978). We run the models up to a depth equivalent to a visual extinction of $A_V \sim 10$ mag. At the back side of the cloud (at $A_V \sim 10$ mag), we use a radiation field 1000 times below that on the front $\chi_{\rm back} = \chi_{\rm front}/1000$. We adopt a cosmic-ray primary ionization rate of $\zeta = 2 \times 10^{-16}$ s^{-1} per H_2 molecule suitable for the dense ISM (Hollenbach et al. 2012).

Figure 9 shows the results of a model for a pressure of 10^8 cm^{-3} K and a radiation field of $\chi_{\rm front} = 1 \times 10^4$, consistent with the radiation field near the ionization front of the Orion Bar. An inclination of 60° was used to extract the line intensities, because of uncertainties in the computation of the line intensities in a 1D model above this value (Gonzalez Garcia et al. 2008). This is reasonably close to the model with 75° inclination suggested to explain the geometry of the Bar (e.g. Melnick et al. 2012). The model with an inclination of 60° reproduces the observed CH^+ line intensities within a factor of 2 for the $J = 1–0$ transition, and with an accuracy of 20% for the other transitions. Our RADEX calculations show the possible importance of electron collisions in the excitation of CH^+. Therefore, to probe the effect of electron collisions on the excitation of CH^+, we implemented CH^+-e^- collisions in the Meudon code. The models for $P = 10^8$ cm^{-3} K and $\chi = 10^4$ are shown in Fig. 9. Including electrons in the excitation of CH^+, the model reproduces the observed line intensities with an accuracy of ~30%. Including electron collisions affects mostly the two lowest-J transitions. The predicted intensity of the $J = 1–0$ transition increases by ~22%, and the intensity of the $J = 2–1$ transition increases by ~18% after including electron collisions.

The CH^+ abundance profile corresponding to this model is shown in Fig. 10 together with the gas temperature in the region

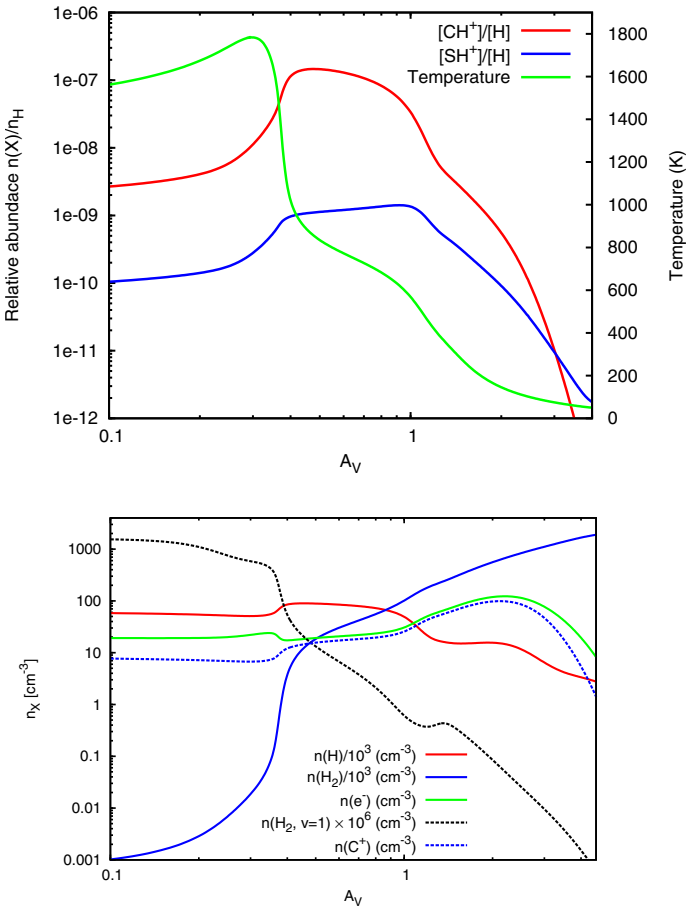

Fig. 10. *Top panel*: CH^+ and SH^+ abundances and the gas kinetic temperature as a function of A_V for a pressure of $P = 10^8$ cm^{-3} K and $\chi = 10^4$. *Bottom panel:* H, H_2, H_2 ($v = 1$), e^-, and C^+ densities.

where CH^+ abundances peak. The model predicts that CH^+ forms near the surface of the PDR ($A_V < 1$) at high temperatures ($T \sim 500$–1000 K), consistent with the predictions by Agundez et al. (2010) and with our RADEX calculations. Though the best fitting models predict abundances to peak near the surface of the cloud at low A_V, the PACS observations of excited CH^+ used in this paper show a spatial extension along the area covered by PACS ($47'' \times 47''$), as shown in Fig. 1. SPIRE observations of the $J = 1$–0 transition (Naylor et al. 2010; Habart et al. 2010) show extended CH^+ emission over a $\sim 200'' \times 200''$ region centered on the $\alpha_{J2000} = 05^h35^m22.83^s$, $\delta_{J2000} = -05°24'57.67''$ position. The CH^+ $J = 1$–0 emission mapped with HIFI was found to extend over a large region covering the OMC-1 cloud (Goicoechea et al., in prep.). One possibility is that the known clumpiness of the Orion Bar extends over a large volume and creates multiple PDR surfaces. Alternative explanation is that the extended CH^+ emission seen toward the region is the result of a not completely edge-on PDR that is tilted to the line of sight. Models with lower pressures under-predict the observed line intensities. For example, a model with a pressure of 5×10^7 K cm^{-3} underpredicts the line intensities with a factor of ~4.

4.3. SH^+ formation

SH^+ forms via a similar reaction to CH^+, however, with an endothermicity about twice as high, $\Delta E = 9860$ K. Since state-to-state formation rates are not available for the $H_2 + S^+ \rightarrow SH^+ + H$ reaction, we use the rates of the $H_2 + C^+ \rightarrow CH^+ + H$ reaction as an approximation, taking into account H_2 rotational levels up to $E_{11} = 10\,261.8$ K and H_2 in the $v = 1$ state up to $E = 10\,341.5$ K. This is a reasonable assumption, since the total rates of the reactions for CH^+ and SH^+ formation via $C^+ + H_2$ and $S^+ + H_2$ are of the same order of magnitude (Woodall et al. 2007). To account for the higher activation barrier, we use $k_{1,\mathrm{mod}} = 1.58 \times 10^{-10} \exp(-[9860 - E_j/k]/T)$. We use the 1.4.4 version of the Meudon code (Le Petit et al. 2006; Goicoechea & Le Bourlot 2007; Le Bourlot et al. 2012), where we introduce the SH^+ formation described above and use scaled radiative rates (J. Black, priv. comm.) and electron-impact collisions calculated in the Coulomb-Born approximation (Black, priv. comm.) for the excitation of SH^+.

With these assumptions, our best fit Meudon PDR model for CH^+ ($P = 10^8$ cm^{-3} K, $\chi = 10^4$) underpredicts the absolute intensities of the observed SH^+ transitions by a factor of ~3.5 for the $F = 5/2 \rightarrow 3/2$ and $F = 3/2 \rightarrow 1/2$ transitions, and by a factor of 6.5 for the $F = 3/2 \rightarrow 3/2$ transition. Owing to the uncertainty in the formation rates, this agreement may be reasonable and suggests that like CH^+, SH^+ can also be formed via H_2 vibrational excitation in warm and dense PDRs. It may also suggest that SH^+ originates in a higher-pressure medium compared to CH^+, which would explain the difference in the observed linewidths. The SH^+ abundances corresponding to this model are shown in Fig. 10. SH^+ abundances, like CH^+ abundances, peak near the surface of the cloud at $A_V \lesssim 1$ at high temperatures (500–1000 K). The SH^+/CH^+ abundance ratio in this region is between 0.01 and 0.1. This, however, is a lower limit on the SH^+/CH^+ abundance ratio, since our model underestimates the SH^+ line intensities.

5. The destruction of CH^+ and SH^+

Figure 11 shows the abundance ratio of CH^+ and SH^+ predicted by our best-fit model in the region where CH^+ and SH^+ abundances peak. To understand these abundance ratios, it is essential to study the destruction of CH^+ and SH^+. CH^+ destruction can follow four main paths in the probed temperature and density regime

$$H + CH^+ \xrightarrow{k_{H,CH^+}} H_2 + C^+$$

$$H_2 + CH^+ \xrightarrow{k_{H_2,CH^+}} H + CH_2^+$$

$$e^- + CH^+ \xrightarrow{k_{e^-,CH^+}} H + C$$

$$h\nu + CH^+ \xrightarrow{k_{h\nu,CH^+}} C + H^+.$$

Unlike CH^+, SH^+ does not react with H_2 at the given physical conditions, as the reaction rate is orders of magnitude lower than that of reactions with electrons and H. Therefore the most important destruction paths are photodissociation as well as chemical reactions with H and electrons

$$H + SH^+ \xrightarrow{k_{H,SH^+}} H_2 + S^+$$

$$e^- + SH^+ \xrightarrow{k_{e^-,SH^+}} H + S$$

$$h\nu + SH^+ \xrightarrow{k_{h\nu,SH^+}} H + S^+.$$

The chemical reaction rates for these reactions are based on Woodall et al. (2007) and are summarized in Table 3.

At a depth equivalent to a visual extinction of $A_V \sim 0.5$, which is in the region where the CH^+ and SH^+ abundances

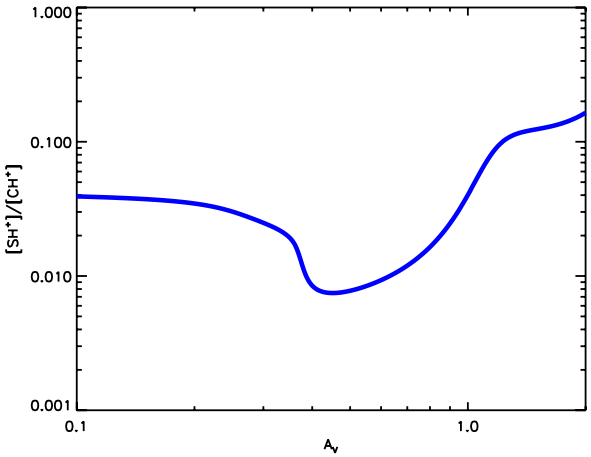

Fig. 11. Abundance ratios of CH^+ and SH^+ in our best fit model ($\chi = 10^4$, $P = 10^8$ cm^{-3} K) in the warm surface region ($A_V < 2$) as a function of depth into the cloud.

Table 3. Rates corresponding to the main destruction paths of CH^+ and SH^+, based on Woodall et al. (2007).

Reaction	Rate ($cm^3\ s^{-1}$)	Temperature regime (K)
k_{H,CH^+}	7.5×10^{-10}	10–41 000
k_{H_2,CH^+}	1.2×10^{-9}	10–41 000
k_{e^-,CH^+}	$1.5 \times 10^{-7} \times (T/300)^{-0.42}$	10–300
k_{H,SH^+}	1.10×10^{-10}	10–41 000
k_{e^-,SH^+}	$2.0 \times 10^{-7} \times (T/300)^{-0.5}$	10–300
Reaction	Rate (s^{-1})	Temperature regime (K)
$k_{h\nu,CH^+}$	$2.50 \times 10^{-10} \exp(-2.5A_V)$	10–41 000
$k_{h\nu,SH^+}$	$3.00 \times 10^{-10} \exp(-1.8A_V)$	10–41 000

peak, and at a temperature of ~830 K, most CH^+ (73.2%) is destroyed via collisions with H, while 24.3% is destroyed via collisions with H_2 and 2.1% is destroyed via collisions with electrons. Photodissociation is negligible in this regime, since it is responsible for 0.4% of the destructions of CH^+. Deeper in the cloud, at a depth equivalent to $A_V \sim 1$, and at a gas temperature of ~570 K, most CH^+ (74.9%) is destroyed by collisions with H_2, while small percentages of CH^+ are destroyed via collisions with H (22.8%), with electrons (2.2%), and by photodissociation (0.6%).

At a depth of $A_V \sim 0.5$, most SH^+ (~77.2%) is destroyed via reactions with H and a smaller percentage is destroyed via reactions with electrons (~18.2%) and by photodissociation (~4.4%). At a depth corresponding to $A_V \sim 1$, SH^+ is almost equally destroyed by reactions with H (~53.3%) and electrons (~43.7%). A smaller percentage of SH^+ is destroyed via photodissociation (~2.4%).

At $A_V \sim 1$ and deeper, the SH^+ and CH^+ abundance ratio becomes higher than 0.1. Deeper in the cloud than $A_V \sim 1$ CH^+ abundances decrease more rapidly than SH^+ abundances. The $[SH^+]/[CH^+]$ abundance ratio varies in the range between 0.01 (at $A_V \sim 0.2$) and >0.1 (at $A_V \sim 1$) and indicate that the destruction of CH^+ becomes more efficient as a function of the depth into the cloud where H_2 takes over as the most important destruction partner, while with the decrease of atomic hydrogen density SH^+ becomes more abundant because electrons are a less efficient destruction partner. While in diffuse clouds the abundance ratios of $[SH^+]/[CH^+]$ trace the importance of shocks (e.g. Menten et al. 2011) and properties of turbulent dissipation regions (e.g. Godard et al. 2012), in clouds exposed to high UV irradiation these abundances are sensitive to the abundance ratios of H, H_2, and electrons as a function of depth into the cloud, which are determined by the radiation field strength of the irradiation source.

6. Discussion

We have analyzed six rotational transitions of CH^+ and three transitions of SH^+ and reported the first detection of the $J = 5–4$ transition of CF^+. We have shown that electron collisions affect the excitation of SH^+ and CH^+, especially the lowest-J transitions. We have also shown the importance of taking reactive collisions into account in the case of CH^+ excitation. We have confirmed, both by an analytic approximation and by more detailed PDR modeling, that CH^+ formation is driven by H_2 vibrational excitation, unlike in the case of diffuse environments with lower UV radiation fields. SH^+ is also likely to form via H_2 vibrational excitation, although the lack of information on the exact state-to-state formation rates introduces an extra uncertainty in the models.

6.1. The formation of CH^+ and SH^+

Spatially extended vibrationally excited H_2 emission was detected in the Orion Bar before the launch of *Herschel* (Van der Werf et al. 1996; Walmsley et al. 2000), already indicating an importance in the chemistry of species that react with H_2. Using *Herschel*, CH^+ was detected in the Orion Bar by Naylor et al. (2010) and Habart et al. (2010), based on SPIRE maps of the 1–0 transition. These observations show extended CH^+ 1–0 emission in the Orion Bar as well as in the OMC-1 cloud (Naylor et al. 2010; P. Morris, priv. comm.; J. Goicoechea, priv. comm.). Naylor et al. (2010) argue that the large spatial extent of CH^+ into regions of low A_V suggests the importance of the formation via H_2 vibrational excitation. Our observations extend these studies, since the additional observed transitions up to $J = 6–5$ provide additional evidence on the importance of the formation via vibrationally excited H_2. An origin of CH^+ in the warm surface regions of the PDR is also confirmed by Goicoechea et al. (2011) who found a spatial correlation between excited OH $^2\Pi_{3/2}$ $J = 7/2^- \rightarrow 5/2^+$ (~84.6 μm, observed with PACS) and CH^+ 3–2 emission, and that OH originates in the surface region ($A_V < 1$) of a high pressure gas component ($10^8–10^9$ K cm^{-3}). The formation and excitation of CH^+ in the Orion Bar is similar to that in the envelope of the high-mass protostar AFGL 2591, as its CH^+ emission can be explained to originate in the FUV-irradiated outflow-walls (Bruderer et al. 2010). Another region where CH^+ formation is driven by the strong FUV radiation field and can be explained by H_2 vibrational excitation is the protoplanetary disc HD 100546 (Thi et al. 2011), where CH^+ emission mostly originates in the outer disc and the disc surface in warm gas ($T_{gas} > 400$ K).

Other explanations for the formation of CH^+ applicable to the diffuse ISM include shocks (e.g. Pineau des Forêts et al. 1986). Tielens et al. (1993) have investigated that shocks do not contribute to the chemistry of the Orion Bar; therefore, we consider this scenario unlikely. Another scenario for CH^+ formation that has been successful in reproducing CH^+ abundances for the diffuse interstellar medium is the dissipation of turbulence (Godard et al. 2009, 2012). Though the CH^+ 1–0 and 2–1 transitions have broader line widths than most dense gas tracers in

the Orion Bar, most of the lines detected in the Orion Bar are narrow (2–3 km s^{-1}); therefore, we find it unlikely that turbulence plays a role in the chemistry of species detected in the Orion Bar.

Unlike CH^+, SH^+ has not been observed in a large variety of regions since its recent discovery in absorption toward Sagittarius B2 (Menten et al. 2011). A recent study by Godard et al. (2012) probes CH^+ and SH^+ in absorption in the diffuse interstellar medium toward high-mass star-forming regions, suggesting a common origin for the formation and excitation of these ions, based on their observed linewidth-distributions and on comparison with MHD shock models. However, in the diffuse ISM, SH^+ and CH^+ abundances are influenced by the dissipation of turbulence. SH^+ has also been detected in emission in the high-mass star-forming region W3 IRS5 (Benz et al. 2010), which represents a region with physical conditions comparable to the Orion Bar, where the UV-radiation of the embedded protostars drives the chemistry of SH^+.

6.2. CH^+ and SH^+ as tracers of the warm PDR surface

Though CH^+ and SH^+ most likely form via the same process and originate in the warm surface region of the PDR, a significant difference between CH^+ and SH^+ emission is suggested by the difference in the observed line widths. While the observed line width of SH^+ ($\Delta v \sim 3$ km s^{-1}) is closer to that of dense gas tracers ($\Delta v \sim 2$–3 km s^{-1}), the width of the CH^+ $J = 1-0$ and 2−1 transitions ($\Delta v \sim 5$ km s^{-1}) is similar to that of HF ($\Delta v \sim 4.9$ km s^{-1}, Van der Tak et al. 2012) and C^+ ($\Delta v \sim 3.8$ km s^{-1}), tracers of the interclump medium. The C91α carbon recombination line was observed with the VLA with a width of 2−2.5 km s^{-1} (Wyrowski et al. 1997). It was found to match the H_2 [1–0 S(1)] distribution (Van der Werf et al. 1996) and its radial velocity was found to be consistent with that of H_2 pure rotational lines H_2 $v = 0$–0 S(1), S(2), and S(4) (Allers et al. 2005). The $^{13}C^+$ lines have a slightly larger width of 2.5−2.8 km s^{-1}, compared to that of the C91α line. The larger width of the [CII] 158 μm line compared to the $^{13}C^+$ lines can be a result of optical depth broadening of the C^+ line (with an optical depth of 2–3). However, the C^+ line is also broader near the edge of the Bar, where the column density of material is lower, as are the line optical depths. In addition, the recombination line intensity is sensitive to the square of the electron density, while the fine structure line is sensitive to the local density only. Therefore the difference in line profiles of the C91α and [CII] 158 μm lines outside opacity broadening may also be related to gradients in the beam and along the line of sight, with the denser material having a lower velocity dispersion.

This possible difference in the properties of the emitting regions is further indicated by our RADEX models (Sect. 3.2). These models reproduce the observed CH^+ line intensities with a temperature of $T = 500-1000$ K and a density of $n \sim 10^5$ cm^{-3}, but suggest a higher density component to explain SH^+ emission, $T \sim 200$ K, $n \sim 10^6$ cm^{-3}, which is consistent with the properties of warm and dense condensations suggested to explain the origin of excited OH (Goicoechea et al. 2011) and high-J CO line emission (Joblin et al., in prep.). In this case, thermal line broadening may contribute to the difference between the widths of the CH^+ and SH^+ lines. The expected contribution of thermal line broadening for CH^+ is $\Delta v = 2\sqrt{2\ln 2}\sqrt{\frac{kT}{m}} = 1.3$ km s^{-1} for $T_{\rm kin} = 500$ K, and $\Delta v = 1.8$ km s^{-1} for $T_{\rm kin} = 1000$ K. The contribution of thermal line broadening for SH^+ for $T_{\rm kin} = 200$ K is $\Delta v = 0.6$ km s^{-1}.

As an alternative explanation of the large observed line width of CH^+, formation pumping may play a role in the broadening of CH^+. As explained in Sect. 3.2, CH^+ formation results in an excess energy equivalent to 5360 K. This energy may be redistributed and go into kinetic motions. If the 5360 K excess energy goes into excess translational energy of the nascent CH^+, and if this is identified as an ionic kinetic temperature upon formation, then the corresponding FWHM of Doppler motions is 4.4 km s^{-1}.

The difference between the widths of CH^+ and SH^+ may not originate in different excitation conditions, but in the difference in the chemistry of these ions. After its formation, CH^+ rapidly reacts with H and H_2, therefore it is likely that its translational motions never become thermalized. In this case, the large velocity dispersion in CH^+ partially reflects the conditions of its formation. SH^+ on the other hand does not react rapidly with H (and H_2), so that it is destroyed less rapidly by recombination with electrons. Therefore, SH^+ can become thermalized translationally during its chemical lifetime. Therefore, while SH^+ traces the density and the temperature of the emitting region, CH^+ is more sensitive to the details of its formation process.

Another interpretation of the broadening of CH^+ and other molecules could be that they originate in flows created by photo-evaporating clumps (e.g. Gorti & Hollenbach 2002; Mackey & Lim 2010). However, our observed data don't completely support this assumption. If the FWHM of ions and other molecules detected at the same position had a contribution by the evaporating flow, we would expect C^+ and CH^+ to have a similar flow velocity, as the momentum transfer from H_2 in the H_2^* + C^+ reaction is small. Based on our HIFI observations of the CO^+ peak, this does not apply, as $FWHM(C^+) \sim 3.8$ km s^{-1} and $FWHM(CH^+) \sim 5$ km s^{-1}.

The difference in the width of reactive ions tracing the warm surface region of the PDR is a key part of understanding the chemistry of these ions. Future observations of the spatial distribution of SH^+ will help to distinguish between these explanations.

6.3. An extension of the "CF^+ ladder" in the orion Bar

Unlike CH^+ and SH^+, CF^+ does not directly form via collisions with H_2. The reaction between fluorine and H_2 is followed by a reaction between C^+ and HF, where HF is the dominant reservoir of fluorine and was previously detected in emission in the Orion Bar by Van der Tak et al. (2012)

$$F + H_2 \rightarrow HF + H$$

$$HF + C^+ \rightarrow CF^+ + H.$$

CF^+ is the second most important fluorine reservoir and accounts for ∼1% of the gas-phase fluorine abundance. However, CF^+ has so far only been detected in two sources. The 2–1 and 1–0 rotational transitions have been recently detected with a spatially extended emission toward the PDR in the Horsehead nebula (Guzman et al. 2012). The first detection of CF^+ was toward the Orion Bar (Neufeld et al. 2006), showing spatially extended emission in the 1–0, 2–1, and 3–2 rotational transitions. Our observations extend the observed CF^+ transitions toward the Orion Bar up to the 5–4 transition and since the line intensity is consistent with the previously observed transitions, this work gives additional confirmation on the simple CF^+ chemistry tracing the surface layers exposed to UV irradiation.

7. Conclusions and outlook

We have analyzed six rotational transitions of CH^+ and three transitions of SH^+ and have reported the first detection of the 5–4 transition of CF^+. Our main conclusions are the following:

- We have detected CH^+ up to the 6–5 transition. The 2–1 and 1–0 transitions are spectrally resolved and show significantly broader lines ($\Delta v \sim 5$ km s^{-1}) than most dense gas tracers in the Orion Bar. SH^+ on the other hand shows significantly narrower lines than CH^+ ($\Delta v \sim 3$ km s^{-1}). Explanations of this difference include their origin in a different density (and temperature) component. Alternatively, because of its reactivity, CH^+ never becomes thermalized. Therefore, its observed properties trace the formation process rather than the properties of the emitting region, unlike for SH^+. Information on the spatial distribution of SH^+ is needed to resolve this puzzle.
- Inelastic collisions with H_2 and electrons both affect the excitation of CH^+ and SH^+, similar to the case of HF (Van der Tak et al. 2012). Reactive collisions are important in the excitation of CH^+, but have less effect in the case of SH^+.
- Comparing the observed CH^+ intensities to predictions of PDR models for typical conditions in the Orion Bar, we confirm that CH^+ forms via reactions with vibrationally excited H_2, as predicted by Agundez et al. (2010). Our PDR models also show that CH^+ forms in the warm surface region ($T \sim 500-1000$ K) of the PDR at high pressures ($\sim 10^8$ cm^{-3} K).
- SH^+ is also likely to form via H_2 vibrational excitation, assuming that the formation rates are similar to that of CH^+. SH^+ is also a tracer of the warm surface regions of the PDR.

In the future, higher-resolution follow-up observations of a larger region in the Orion Bar will give more insight into the excitation conditions of SH^+. Probing CH^+ and SH^+ formation in PDRs with a range of parameters, such as different radiation fields would help to deepen our understanding of the chemistry of these ions in regions exposed to UV irradiation.

Acknowledgements. We thank the referee for the constructive suggestions that helped to improve the paper. We also thank the editor Malcolm Walmsley for additional comments. We thank Simon Bruderer for useful comments on CH^+ and SH^+ and Yunhee Choi for the help in the reduction of the HIFI data. J.R.G. is supported by a Ramón y Cajal research contract; he thanks the Spanish MINECO for funding support through grants AYA2009-07304 and CSD2009-00038. Support for this work for E.A.B. was provided by NASA through an award issued by JPL/Caltech. Part of the work was supported by the *Deutsche Forschungsgemeinschaft* through grant SFB 956 C1. HIFI was designed and built by a consortium of institutes and university departments from across Europe, Canada, and the US under the leadership of SRON Netherlands Institute for Space Research, Groningen, The Netherlands, with major contributions from Germany, France, and the US. Consortium members are Canada: CSA, U.Waterloo; France: IRAP, LAB, LERMA, IRAM; Germany: KOSMA, MPIfR, MPS; Ireland: NUIMaynooth; Italy: ASI, IFSI-INAF, Arcetri-INAF; The Netherlands: SRON, TUD; Poland: CAMK, CBK; Spain: Observatorio Astronomico Nacional (IGN), Centro de Astrobiología (CSIC-INTA); Sweden: Chalmers University of Technology – MC2, RSS & GARD, Onsala Space Observatory, Swedish National Space Board, Stockholm University – Stockholm Observatory; Switzerland: ETH Zürich, FHNW; USA: Caltech, JPL, NHSC. HIPE is a joint development by the *Herschel* Science Ground Segment Consortium, consisting of ESA, the NASA *Herschel* Science Center, and the HIFI, PACS, and SPIRE consortia. PACS was developed by a consortium of institutes led by MPE (Germany) and including UVIE (Austria); KU Leuven, CSL, IMEC (Belgium); CEA, LAM (France); MPIA (Germany); INAFIFSI/OAA/OAP/OAT, LENS, SISSA (Italy); IAC (Spain).

References

Agúndez, M., Goicoechea, J. R., Cernicharo, J., et al. 2010, ApJ, 713, 662
Allers, K. N., Jaffe, D. T., Lacy, J. H., Draine, B. T., & Richter, M. J. 2005, ApJ, 630, 368
Benz, A. O., Bruderer, S., van Dishoeck, E. F., et al. 2010, A&A, 521, A35
Bergin, E. A., Phillips, T. G., Comito, C., et al. 2010, A&A, 521, L20
Bruderer, S., Benz, A. O., van Dishoeck, E. F., et al. 2010, A&A, 521, L44
Coutens, A., Vastel, C., Caux, E., et al. 2012, A&A, 539, A132
De Graauw, T., Helmich, F. P., Phillips, T. G., et al. 2010, A&A, 518, L6
Douglas, A. E., & Herzberg, G. 1941, ApJ, 94, 381
Draine, B. T. 1978, ApJS, 36, 595
Falgarone, E., Godard, B., Cernicharo, J., et al. 2010a, A&A, 521, A15
Falgarone, E., Ossenkopf, V., Gerin, M., et al. 2010b, A&A, 518, A118
Fuente, A., Rodríguez-Franco, A., García-Burillo, S., et al. 2003, A&A, 406, 899
Gerlich, D., Disch, R., & Scherbarth, S. 1987, J. Chem. Phys., 87, 350
Godard, B., Falgarone, E., & Pineau Des Forêts, G. 2009, A&A, 495, 847
Godard, B., Falgarone, E., Gerin, M., et al. 2012, A&A, 540, A87
Goicoechea, J. R., & Le Bourlot, J. 2007, A&A, 467, 1
Goicoechea, J. R., Joblin, C., Contursi, A., et al. 2011, A&A, 530, L16
Gonzalez Garcia, M., Le Bourlot, J., Le Petit, F., & Roueff, E. 2008, A&A, 485, 127
Gorti, U., & Hollenbach, D. 2002, ApJ, 573, 215
Griffin, M. J., Abergel, A., Abreu, A., et al. 2010, A&A, 518, L3
Guzmán, V., Pety, J., Gratier, P., et al. 2012, A&A, 543, A1
Habart, E., Dartois, E., Abergel, A., et al. 2010, A&A, 518, L116
Hierl, P. M., Morris, R. A., & Viggiano, A. A. 1997, J. Chem. Phys., 106, 10145
Hogerheijde, M. R., Jansen, D. J., & Van Dishoeck, E. F. 1995, A&A, 294, 792
Hollenbach, D., Kaufman, M. J., Neufeld, D., Wolfire, M., & Goicoechea, J. R. 2012, ApJ, 754, 105
Le Bourlot, J., Le Petit, F., Pinto, C., Roueff, E., & Roy, F. 2012, A&A, 541, A76
Le Petit, F., Nehmé, C., Le Bourlot, J., & Roueff, E. 2006, ApJS, 164, 506
Lim, A. J., Rabadán, I., & Tennyson, J. 1999, MNRAS 306, 473
Lis, D. C., & Schilke, P. 2003, ApJ, 597, 145
Lis, D. C., Serabyn, E., Keene, J., et al. 1998, ApJ, 509, 299
Mackey, J., & Lim, A. J. 2010, MNRAS, 403, 714
Magnani, L., & Salzer, J. J. 1989, AJ, 98, 926
Magnani, L., & Salzer, J. J. 1991, AJ, 101, 1429
Melnick, G., Tolls, V., Goldsmith, P., et al. 2012, ApJ, 752, 26
Menten, K. M., Reid, M. J., Forbrich, J., & Brunthaler, A. 2007, A&A, 474, 515
Menten, K. M., Wyrowski, F., Belloche, A., et al. 2011, A&A, 525, A77
Millar, T. J., & Hobbs, L. M. 1988, MNRAS, 231, 953
Müller, H. S. P., Schöder, F., Stutzki, J., & Winnewisser, G. 2005, J. Mol. Struct., 742, 215
Müller, H. S. P. 2010, A&A, 514, L6
Naylor, D. A., Dartois, E., Habart, E., et al. 2010, A&A, 518, L117
Neufeld, D. A., Schilke, P., Menten, K. M., et al. 2006, A&A, 454, L37
Ossenkopf, V., Röllig, M., Neufeld, D. A., et al. 2013, A&A, 550, A57
Ott, S. 2010, in Astronomical Data Analysis Software and Systems XIX, eds. Y. Mizumoto, K.-I. Morita, & M. Ohishi, ASP Conf. Ser., 434, 139
Pilbratt, G. L., Riedinger, J. R., Passvogel, T., et al. 2010, A&A, 518, L1
Pineau des Forêts G., Flower, D. R., Hartquist, T. W., & Dalgarno, A. 1986, MNRAS, 220, 801
Poglitsch, A., Waelkens, C., Geis, N., et al. 2010, A&A, 518, L2
Roelfsema, P., Helmich, F., Teyssier, D., et al. 2012, A&A, 537, A17
Röllig, M., Ossenkopf, V., Jeyakumar, S., Stutzki, J., & Sternberg, A. 2006, A&A, 451, 917
Schöier, F. L., Van der Tak, F. F. S., Van Dishoeck, E. F., & Black, J. H. 2005, A&A, 432, 369
Simon, R., Stutzki, J., Sternberg, A., & Winnewisser, G. 1997, A&A, 327, 9
Sternberg, A., & Dalgarno, A. 1995, ApJS, 99, 565
Störzer, H., Stutzki, J., & Sternberg, A. 1995, A&A, 296, L9
Thi, W.-F., Ménard, F., Meeus, G., et al. 2011, A&A, 530, L2
Tielens, A. G. G. M., Meixner, M. M., van der Werf, P. P., et al. 1993, Science, 262, 86
Turpin, F., Stoecklin, T., & Voronin, A. 2010, A&A, 511, A28
Van Dishoeck, E. F., & Black, J. H. 1986, ApJS, 62, 109
Van der Tak, F. F. S., Black, J. H., Schöier, F. L., Jansen, D. J., & van Dishoeck, E. F., 2007, A&A, 468, 627
Van der Tak, F. F. S., Ossenkopf, V., Nagy, Z., et al. 2012, A&A, 537, L10
Van der Werf, P., Stutzki, J., Sternberg, A., & Krabbe, A. 1996, A&A, 313, 633
Van der Wiel, M. H. D., Van der Tak, F. F. S., Ossenkopf, V., et al. 2009, A&A, 498, 161
Walmsley, C. M., Natta, A., Oliva, E., & Testi, L. 2000, A&A, 364, 301
Woodall, J., AgÃžndez, M., Markwick-Kemper, A. J., & Millar, T. J. 2007, A&A, 466, 1197
Wyrowski, F., Schilke, P., Hofner, P., & Walmsley C. M., 1997, ApJ, 487, L171
Young Owl, R. C., Meixner, M. M., Wolfire, M., Tielens, A. G. G.M., & Tauber, J. 2000, ApJ, 540, 886